International Journal of Coal Geology 253 (2022) 103950

Contents lists available at ScienceDirect

International Journal of Coal Geology

journal homepage: www.elsevier.com/locate/coal

Probing oil recovery in shale nanopores with small-angle and ultra-small-angle neutron scattering

Chelsea W. Neil [a,*], Rex P. Hjelm [b,l], Marilyn E. Hawley [c], Erik B. Watkins [d], Cody Cockreham [a,e,f], Di Wu [e,f,g,h], Yimin Mao [i,j], Michael Cheshire [k], Jon Burger [k], Timothy B. Fischer [k], M. Rebecca Stokes [k,1], Hongwu Xu [a]

[a] Earth and Environmental Sciences Division, Los Alamos National Laboratory, Los Alamos, NM 87545, USA
[b] National Security Education Center, Los Alamos National Laboratory, Los Alamos, NM 87545, USA
[c] Materials Science and Technology Division (Retired), Los Alamos National Laboratory, Los Alamos, NM 87545, USA
[d] Materials Physics and Applications, Los Alamos National Laboratory, Los Alamos, NM 87545, USA
[e] Voiland School of Chemical Engineering and Bioengineering, Washington State University, Pullman, WA 99164, USA
[f] Alexandra Navrotsky Institute for Experimental Thermodynamics, Washington State University, Pullman, WA 99164, USA
[g] Materials Science and Engineering, Washington State University, Pullman, WA 99164, USA
[h] Department of Chemistry, Washington State University, Pullman, WA 99164, USA
[i] Department of Materials Science and Engineering, University of Maryland, College Park, MD 20742, USA
[j] NIST Center for Neutron Research, National Institute of Standards and Technology, Gaithersburg, MD 20899, USA
[k] Chevron Technology Center, 3901 Briarpark Drive, Houston, TX 77042, USA
[l] The New Mexico Consortium, Los Alamos, NM 87544, USA

ARTICLE INFO

Keywords:
Shale
Enhanced oil recovery
Neutron scattering
Nanoporosity

ABSTRACT

Increasing oil production from unconventional shale reservoirs is crucial to meet growing energy demands while achieving lower carbon emission than conventional crude oil. Enhanced oil recovery (EOR) has been proposed to improve hydrocarbon recovery rates through the injection of a fluid into the reservoir to facilitate residual oil release from the shale formation. However, economical and sustainable implementation of EOR requires advanced knowledge of fluid behavior in nano-sized pore spaces in shale. In this study, we utilize small-angle neutron scattering (SANS) and ultra-small-angle neutron scattering (USANS) as experimental probes to examine decane removal from a shale nano- to micro-porous matrix, utilizing methane as the injectant. The extent of decane saturation and recovery post-methane pressurization is quantified for clay-rich and carbonate-rich shale samples. A key finding is that extraction of decane by methane on depressurization is related to the methane-decane critical point. Furthermore, we found that although clay-rich shale had a much higher porosity of 5.6%, compared with 1.2% for carbonate-rich shale, decane was more easily removed from the carbonate-rich matrix, leading to similar hydrocarbon yields. These promising results demonstrate the ability of SANS and USANS to provide key insights into oil recovery from nano- to micron-sized pores in shale matrices. Combined with effects of various fractures on fluid behavior in shale, this experimental technique can be used to assess the viability of EOR injectants.

1. Introduction

Unconventional oil from tight shale formations has the potential to provide consumers with cleaner energy and reduce the US's reliance on energy imports (Kerr, 2010; Paltsev et al., 2011; Wang et al., 2014). Over the past decade, shale oil production has increased from less than 0.5 million barrels per day to over 4 million barrels per day (Kilian, 2016). However, the U.S. still imports half of its utilized oil to meet demands, and shale oil production is predicted to decline in the 2020s, barring the discovery of new resources or improved recovery technology (US Energy Information Administration, 2019).

Upon drilling of a well, production generally declines hyperbolically

---

[*] Corresponding author at: P.O. Box 1663, Los Alamos, NM 87545, USA.
E-mail address: cwneil@lanl.gov (C.W. Neil).

[1] Current affiliation: Geology, Energy and Minerals Science Center, U.S. Geological Survey, Reston, VA 20192, USA.

https://doi.org/10.1016/j.coal.2022.103950
Received 15 July 2021; Received in revised form 15 January 2022; Accepted 4 February 2022

due to limited diffusion of hydrocarbons from nanopores in the shale matrix. As a result, overall hydrocarbon recovery rates using existing methods are less than 10% for oil and approximately 20% for gas (Dong et al., 2013). One proposed improvement for oil recovery is enhanced oil recovery (EOR), whereby a secondary substance is injected into an existing oil well to increase pressure and reduce oil viscosity, allowing for more efficient extraction of the oil as the injection pressure is decreased (pressure drawdown). However, sustainable and economical implementation of EOR strategies requires improved understanding of hydrocarbon interactions and transport behavior in shale nanopores, where a majority of the targeted hydrocarbons are stored (Ma and Jamili, 2016).

Liquid and gaseous hydrocarbons in tight shale formations are formed through the thermal decomposition of kerogen, organic matter found in sedimentary rocks that is insoluble in organic solvents or mineral acids or bases. Depending on the shale thermal maturity, kerogen decomposition can produce varying quantities of oil and gas. In general, less mature formations will produce oil and more mature formations will produce gas (Dembicki, 2016), while a combination of oil and gas will be produced at intermediate maturities. Furthermore, the quantity and type of kerogen can impact the relative presence of oil and gas. For example, Type I kerogen (derived from ancient lakes) and Type II kerogen (derived from marine organic matter) tend to be oil generative, while Type III kerogen (derived from terrestrial organic matter) is considered gas generative (Tissot et al., 1974). However, Types I and II kerogen also produce 1.8 times more gas than Type III kerogen during pyrolysis testing, making it crucial to consider the co-presence of gas in improving oil recovery from oil-generative formations containing Type I and II kerogen (Cardott, 2012).

The coexistence of oil and gas within unconventional reservoirs provides a unique opportunity to utilize coincident gas production for improved oil recovery through gas reinjection. Operators at times limit oil production from wells to reduce associated gas production due to gas pipeline limitations. Enabling a more beneficial use of this resource by recycling methane as the secondary injected EOR substance requires demonstration of the viability of this approach. Additionally, work on methane injection provides further precedent for EOR by CO_2 gas injection, complementing previous research showing the potential for utilizing CO_2-rich gas streams as an EOR injectant (Kuuskraa et al., 2013; Van Bergen et al., 2004; Orr and Taber, 1984). This method has the secondary benefit of providing carbon capture and storage, as a sink to lower CO_2 emissions (Aycaguer et al., 2001; Melzer, 2012). Our objective is thus to experimentally assess oil recovery from shale pores over the micrometer to nanometer sizes in shale with different compositions by directly measuring the extraction of a model hydrocarbon, decane, from shale pores with pressurized methane.

Experimental validation of oil recovery from a shale matrix is challenging, as few techniques can measure response at the nanoscale resolutions necessary to infer the structures of shale pores and the properties of confined fluids without disturbing their essential characteristics. As a result, most current knowledge of fluid behavior in shale nanopores has been obtained via computer simulations (Teklu et al., 2014). Experimental measurements are needed to validate these theoretical observations. Small-angle neutron scattering (SANS) and ultra-small-angle neutron scattering (USANS) techniques are uniquely capable of providing in situ measurement of the relevant structure and properties of geo-materials under controlled sample environments, allowing for examination of pore structure and fluid behavior under a variety of oil recovery scenarios. SANS/USANS thus provide an essential component for synergy between validation of models and the use of models in the analysis and interpretation of experimental measurements.

The choice of SANS/USANS as probes for nanopore structure and properties of geo-materials derives from its unique capabilities. The wavelengths used in the collimated cold neutron beam and the instrument acceptance angle of the scattered beam enable SANS to measure length scales from less than one nm to 100 nm. The unique geometry of the USANS instruments extends this domain to approximately 3 μm. Furthermore, because neutrons are highly penetrating, they are ideal for interrogating materials in robust sample environments, such as pressure cells (Hjelm et al., 2018). Thus, these neutron scattering techniques can be used to probe changes in nanopores at high pressures, allowing for direct comparison with field conditions at shale hydraulic fracturing wells. These scattering methods have been used previously to characterize the structure and connectivity of shale nanopores from various shale reservoirs (Ruppert et al., 2013a; Mang et al., 2000; Clarkson et al., 2013; Gu and Mildner, 2016; King Jr et al., 2015; Mastalerz et al., 2012; Xu, 2020; Neil et al., 2020a). In the current study, we employ SANS and USANS analyses to measure both the accessibility of shale nanopores to decane, a surrogate for target oil hydrocarbons, and the residual decane after pressurizing and then depressurizing the system with methane in a high pressure cell to mimic the oil recovery process. We use mixtures of deuterated and protonated decane, so that the scattering length density (SLD) of filled pores, ρ_p, is contrast matched to the SLD of the shale matrix, ρ_m; thus, the scatter becomes dominated by the decane-inaccessible, unfilled pores. By compariing the porosity of saturated samples to the porosity calculated from the scattering of samples not imbibed with contrast-matched decane, this technique provides a sensitive probe of the populations of decane-accessible and decane-inaccessible pores over the course of the methane depressurization process.

The results show increased decane retention in clay-rich shale compared with carbonate-rich shale. However, clay-rich shale also has significantly higher decane imbibition, likely due to its higher organic matter content. These first-of-a-kind results provide a useful stage to further evaluate different oil recovery scenarios. These results also establish SANS and USANS as a technique for potentially assessing EOR at nanoscale. The efficacy of other gases, such as supercritical CO_2, as potential EOR injectants can also be investigated.

2. Experimental methods[2]

2.1. Sample characterization

Two shale samples with differing mineral compositions were obtained from Chevron: Shale A (carbonate-rich) and Shale B (clay-rich). These shales are from the Permian Basin and were previously used for SANS characterization of pore accessibility to water (Neil et al., 2020a). To determine their mineral compositions, X-ray diffraction (XRD) was conducted using a Siemens D-5000 diffractometer and the data were processed using Chevron's proprietary QUANTA software to quantify mineral percentages in these samples. Samples were spiked with 0.10 g/g zincite as an internal standard prior to milling with a McCrone mill for quantitative XRD analysis. Total Organic Carbon (TOC) content was measured at Weatherford Laboratories, Houston, TX, using LECO TOC and RockEval II pyrolysis. TOC values were converted to organic matter (OM) by dividing by a factor of 0.833, the average carbon concentration reported in Jarvie (Jarvie, 1991). Calculated OM content was then incorporated into the XRD quantification of mineral phases.

The two samples were also measured using Differential Scanning Calorimetry (DSC) / Thermogravimetric Analysis (TGA) to determine their water and carbon contents. This technique has been used previously to study volatile-bearing samples (Guo and Xu, 2017; Xu et al., 2000; Xu et al., 2001). For this measurement, approximately 15 mg of shale powders were packed in a standardized Pt crucible, placed into the calorimeter under an Ar atmosphere and heated to 1273 K at a rate of 10 K/min. The instrument was calibrated using the melting points of In and

---

[2] The identification of any commercial product or trade name does not imply endorsement or recommendation by the National Institute of Standards and Technology.

Table 1
Values used for SLD calculation. Composition of clay-rich and carbonate-rich shales (wt%) was determined by QXRD measurement.

	Calcite[a]	Dolomite/ ankerite[a]	*Total Carbonate*	Quartz[a]	K-feldspar[b]	Plagioclase[b]	Pyrite[a]	Fluorapatite[c]	Organic Matter[b]	*Total Non-clay*	Illite-smectite[a] (<5%Smectite)	Total Clay	*Total*
SLD (×10^{10} cm^{-2})	*4.69*	*5.4*		*4.18*	*3.71*	*3.95*	*3.81*	*4.34*	*3.85*		*2.95*		
Density (g/cm^3)	*2.71*	*2.84*		*2.65*	*2.6*	*2.61*	*5.01*	*3.12*	*1.3*		*2.75*		
Shale A (wt%)	1	1	***2***	52	4	4	2	3	5	***71***	29	29	***100***
Shale A (vol%)	1	1	***2***	50	4	4	1	2	10	***71***	27	27	***100***
Shale B (wt%)	85	6	***91***	4	0	3	0	1	0	***99***	1	1	***100***
Shale B (vol%)	85	6	***91***	4	0	3	0	1	0	***99***	1	1	***100***

[a] SLD and density values from Clarkson et al., 2012, *Fuel*, *95*, pp. 371–385.
[b] SLD and density values from Sun et al., 2018, *International Journal of Coal Geology*, 186, pp. 115–125.
[c] SLD calculated using NIST CNR scattering length density calculator (https://www.ncnr.nist.gov/resources/activation/).

Al metal standards, and sensitivity calibration was conducted using the heat capacities of sapphire. Baseline correction used measurements of an empty Pt crucible run under the same conditions.

X-ray computed tomography (XCT) was used to reconstruct 3D tomographic images of the samples for visualization of shale heterogeneity (Hirono et al., 2008). In XCT, the X-ray beam is attenuated to different extents by the shale density and composition. Low electron density, low Z components of shale, such as organic matter, appear darker in 3D tomographic reconstructions due to having low X-ray attenuation, while high density components, such as pyrite, are bright. XCT scans were performed on Shale A and B sample cores, 2.54 cm to 3.81 cm in diameter and 2.54 cm to 5.08 cm in length. The color scale in these reconstructions represents X-ray attenuation.

2.2. *Calculating scattering length density*

Scattering intensity is proportional to the square of the Fourier transform of the sample structure, given as the variation in the neutron scattering length density (SLD), ρ, with position, $\mathbf{r}$, in the sample. The SLD is defined as the sum of the nuclear scattering lengths, b_i (cm), of atoms present in a given component at position, $\mathbf{r}$, within its volume, V (cm^{-3}), as:

$$\rho = \frac{\sum_i b_i}{V} \left(\mathrm{cm}^{-2}\right) \tag{1}$$

The relation of the scattering intensity to the squared Fourier means that it is proportional to $\overline{\Delta\rho^2}$, the average of the square of the difference in SLD separated by a distance, r, over all r in the sample volume. The values for b, which are proportional to the scattered wave amplitude, vary considerably both between different isotopes, such as hydrogen and deuterium, and also between adjacent elements on the periodic table, giving rise to light element contrast. Thus, SANS/USANS measurements are sensitive to the distribution of organics, minerals and imbibed fluids. By using the difference in the neutron scattering length between deuterium and hydrogen in gas and liquid fluids, this method can clearly discriminate fluid accessible, open pores from inaccessible, closed pores, making it unique among typical porosity measurement techniques (Ruppert et al., 2013a; Mang et al., 2000).

For our system the contrast between pores and the matrix is,

$$\Delta\rho = \rho_p - \rho_m \tag{2}$$

here, p indicates the pore SLD and m refers to the matrix SLD. For presumed empty pores, ρ_p is zero. For the conditions studied here, the strongest scattering thus comes from the difference between empty pores and the shale matrix. The later typically has a ρ value between 3×10^{10} cm^{-2} and 4×10^{10} cm^{-2} (Table 1). As accessible pores are filled with fluid, which has a positive SLD, their SLD increases towards that of the shale matrix, decreasing $\Delta\rho$, and thus the overall scattering intensity. This phenomenon allows for contrast matching, a technique whereby pores are filled with a solution that has the same average SLD as the matrix. Thus, the contribution to scattering of filled pores becomes negligible relative to the inaccessible pores, allowing for clear delineation of accessible vs. inaccessible pores.

2.3. *Small-Angle Neutron Scattering (SANS) and Ultra-Small-Angle Scattering (USANS) measurements*

SANS experiments were conducted on the NG7 30 m SANS instrument at the NIST (National Institute of Standards and Technology) Center for Neutron Research (NCNR) (Glinka et al., 1998). The incident neutron wavelength, λ, was 6 Å with a resolution, $\Delta\lambda/\lambda$, of 13%. Sample-to-detector distances of 1, 4 and 13 m were used, giving a Q (scattering wave number, $Q = 4\pi/\lambda \sin\theta$, with θ being half of the scattering angle) range of 0.003 to 0.43 Å^{-1}. NIST's SANS/USANS data reduction package

(Kline, 2006) was used to radially average the scattering intensity for given scattering angles, converting the data to differential cross sections per steradian per unit volume (cm^{-1}) as a function of Q ($Å^{-1}$), after subtraction of background scattering from the empty pressure cell or ambient sample holder, as needed. In the case of the clay-rich scale, slight anisotropy was accounted for by confirming that the power law remains constant over the major and minor axes of the scattering ellipse, as described in our previous publication, allowing us to simplify analysis by radially-averaging the intensity (Neil et al., 2020a).

USANS data was used to extend the measured Q range of 0.00003–0.003 $Å^{-1}$, allowing for determination of features between 30 nm and 3 μm in size. USANS was conducted using the BT-5 perfect crystal instrument at the NCNR (Barker et al., 2005). The monochromatic incident neutron beam wavelength, λ, was 2.4 Å. Unlike SANS, which uses pinhole collimation and a 2D detector, USANS uses a Bonse-Hart configuration where both the collimator and analyzer have line geometry defined by crystals acting as narrow slit apertures. As a consequence, USANS data is "slit smeared" due to angular collimation in one direction. While this slit smearing is corrected for using NIST's USANS data reduction package, interpretation is further complicated by anisotropic scattering in the clay-rich shale. Due to the USANS slit geometry, scattering cannot simply be radially averaged as it is for SANS. Instead, the USANS intensity was corrected using the method established by Gu and Mildner (Gu and Mildner, 2018). Detailed information and calculations related to this scattering intensity correction can be found in the supporting information (SI).

Shale samples used for SANS and USANS consist of 300 μm thin sections mounted on 3/8″ (9.525 mm) diameter, 1 mm thick silica glass with epoxy at the edges allowing sufficient clearance for the ¼" (6.35 mm) neutron beam diameter used for measurements with the high pressure cell. The sample thickness and SANS incident beam wavelength were chosen to reduce neutron multiple scattering. Using the volume percentages of mineral compositions in Table 1, the SLD was calculated to be 3.81×10^{10} cm^{-2} for clay-rich (A) shale and 4.67×10^{10} cm^{-2} for carbonate-rich (B) shale. Mixtures of hydrogenated decane (SLD $= -0.488 \times 10^{10}$ cm^{-2}) and deuterated decane (SLD $= 6.58 \times 10^{10}$ cm^{-2}) were used as the imbibed oil phase to match the contrast of filled pores with the matrix. These were 60.8% deuterated decane for Shale A and 73.0% deuterated decane for Shale B, giving $\Delta\rho \approx 0$ for the filled pores, as discussed above.

Samples were first measured dry in order to determine the total scattering from empty pores. They were then saturated with the contrast-matched decane mixture under vacuum for three hours. We used SANS to determine that this time was sufficient for the thin sample to be fully saturated, as outlined in the SI. SANS from the saturated samples was then measured at ambient pressure. Because the oil is contrast-matched, scattering remaining after saturation is assumed to be from inaccessible pores.

The decane-saturated samples were pressurized with deuterated methane (CD_4) gas (Cambridge Isotopes Laboratory Inc., Andover MA, USA) in a high-pressure cell designed by NCNR for SANS and USANS measurements. Gas pressure was applied using two ISCO 100HLf continuous flow pumps in tandem (Teledyne/ISCO. Lincoln, NE, USA). The pressurization process was controlled and the pressure data logged by an NCNR-developed LabView (National Instruments, Austin, TX, USA) program. SANS and USANS measurements were made at room temperature with CD_4 pressures over increments of 1500 psi (10.3 MPa) up to 7500 psi (51.7 MPa). Additional measurements were then made while decreasing pressure by 1500 psi (10.3 MPa) increments, with a final measurement under ambient conditions. Due to the long measurement time of approximately 6 h per pressure point, USANS was conducted using a limited pressure cycle, with measurements taken at ambient dry conditions, ambient saturated conditions, then at 1500 psi (10.3 MPa), 4500 psi (31.0 MPa), 7500 psi (51.7 MPa), and back down through the sequence of pressures to ambient. During EOR in the field, this gas injection cycle will occur after primary depletion. However, due to limited beamtime availability, shale samples were put through only one methane pressure cycle. While this may result in more removable decane, we expect that trends in removability and observations of methane-decane interactions occurring in nanopores will translate to the field. In addition, these first-of-their-kind measurements serve as a proof of principle that SANS can be used to observe methane-decane interactions at high pressure in shale nanopores. It should be reiterated that the recovery process emulated here is for the shale matrix only, not considering various sizes of fractures in shale formations. The fracture network plays significant roles in the oil recovery process, especially at the early stage.

Deuterated methane is used to mitigate changes in intensity from its introduction into the pores, which can obscure the decane signal. Methane is expected to enter the same pores accessible to decane, as well as others that are not as accessible to decane due to its smaller molecular size and the application of pressure. The bulk SLD of CD_4 varies with pressure from *ca* 1.1×10^{10} cm^{-2} at 1500 psi (10.3 MPa) to *ca* 3.5×10^{10} cm^{-2} at 7500 psi (51.7 MPa). On this basis, we might expect decreasing contrast of the CD_4 accessible pores relative to the matrix (Eq. (2)), as observed by Ruppert et al. (Ruppert et al., 2013b), and perhaps some contrast increase in decane filled pores from CD_4 mixing with decane. These nuanced effects on the measurements using CD_4 are small in comparison with those expected for protonated methane, where the bulk SLD is -0.25×10^{10} cm^{-2} at 1500 psi (10.3 MPa) to *ca* -0.73×10^{10} cm^{-2} at 7500 psi (51.7 MPa), giving rise to much higher contrast relative to the matrix. Furthermore, the large neutron incoherence of protons in CH_4 will further obscure the pore scatting, particularly for small-scale features probed over high-Q.

2.4. *Size distribution analysis*

Changes in the pore structure and the accessibility to contrast matched n-decane was assessed by calculating the apparent pore size distribution function, PDF. After the scattering data was reduced, curves were fit using the Irena SAS "Size Distribution" macro with the Maximum Entropy (MaxEnt) method implemented in Igor Pro 7 (V. 7.0.8.1) (Ilavsky and Jemian, 2008).

$P_A(R)$, is taken as a continuous function of the fractional density (cm^{-1}) of pores between radii R and $R + dR$ that contribute to the observed SANS data. Here, we apply two simplifying approximations: first, that the pores are spherical, which is built into the Irena PDF tool, and second, that sources of contrast, $\overline{\Delta\rho^2}$, other than empty voids make negligible contributions to the SANS intensity. It is known that the voids have an elliptical shape with the large axis extending along the shale bedding plane (Gu and Mildner, 2016; Gu and Mildner, 2018; Gu et al., 2015), rather than spherical. However, the spherical assumption is not expected to significantly affect quantification of relative changes in the PDF (Neil et al., 2020a). The apparent PDF, $P_A(R)$, is related to a reference PDF as,

$$P_A(R) = \overline{\Delta\rho^2(R)} P_R(R) \tag{3}$$

where $P_R(R)$ is the PDF in the dry, reference state and $\overline{\Delta\rho^2(R)}$ is the average squared contrast of pores of radius between R and $R + dR$, relative to the local matrix environment. Based on the assumption that the injection of n-decane and CD_4 does not alter the $P_R(R)$, any changes in the apparent PDF must reflect the proportion of pores in that size range that are filled with fluid.

Given these considerations, the SANS intensity, $I(Q)$, defined as the differential cross section per steradian per unit volume (cm^{-1}), is a sum of the contribution of scatter from each population of voids with size on the interval, R to $R + dR$, represented as the integral:

$$I(Q) = N_T \int P_A(R) I(R, Q) dR \tag{4}$$

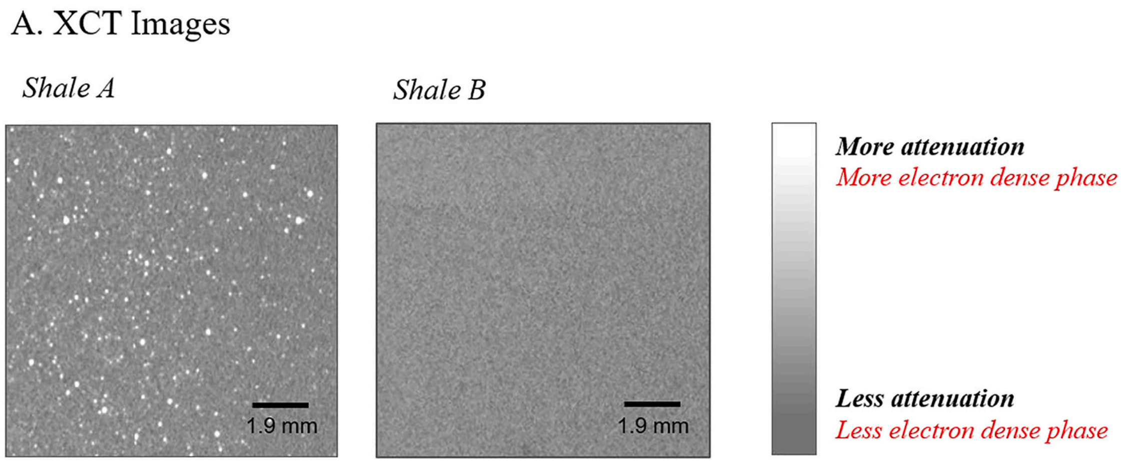

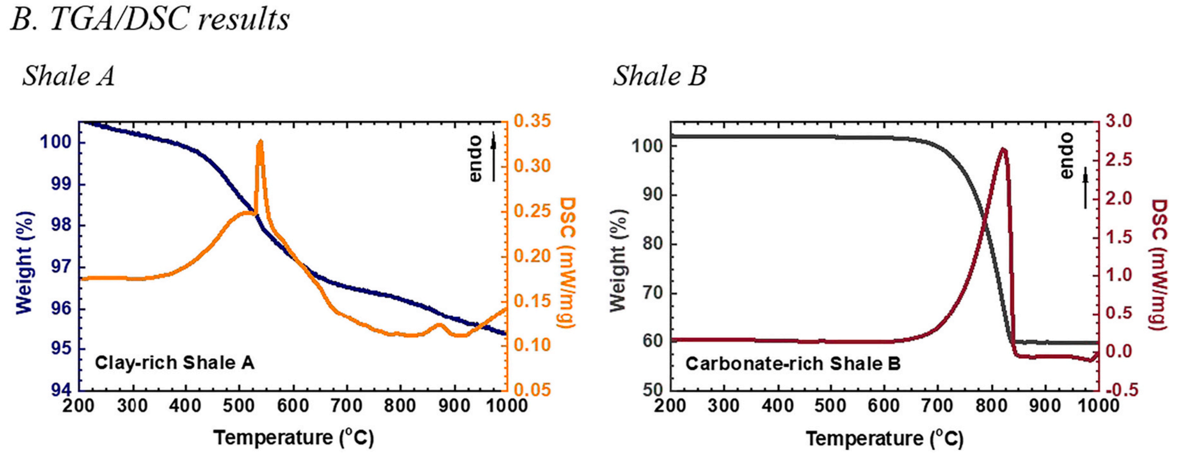

Fig. 1. (A) XCT characterization and (B) TGA/DSC of clay-rich and carbonate-rich shales. Republished with permission from Neil et al. (Neil et al., 2020a)

In Eq. (4), N_T is the number density of pores (cm^{-3}); and I(R,Q) is the scattering intensity from a single pore of radius, R at a given Q. The scattering intensity from a single pore, I(Q,R), (cm^2) is calculated as:

$$I(Q,R) = \Delta\rho^2(R)V^2(R)F(R,Q) \tag{5}$$

here, V is the pore volume and F is the form factor (the scattering from) of a single sphere. The spherical pore assumption is reasonable because the samples are cut approximately parallel to the bedding plane (Gu et al., 2015; Gu et al., 2016); thus, the view of the mainly elliptical voids is circular. The scatter then is a cross section of the squared Fourier transform perpendicular to the semi-major axis. While this approach, which is unavoidable using the Irena tool, might distort the reference PDF, it will not affect the change in $\overline{\Delta\rho^2(R)}$ (Eq. (2)). Although the clay-rich shale sample had some anisotropy, we show in our previous publication that elliptical scattering can be radially-averaged to simplify the analysis (Neil et al., 2020a).

2.5. MaxEnt procedure and sky background

At low Q, scattering from shale obeys a power law such that:

$$I(Q) \sim Q^{-\alpha} \tag{6}$$

The pore size distribution fitting procedure subtracts the background and power law scattering, under the assumption that low Q scattering results from large-scale structures not associated with the pore size distribution (e.g. pore surface roughness, correlated distances, *etc*) (Ilavsky and Jemian, 2008). The residual intensity is then used to determine $P_A(R)$. Fitted residual intensities can be found in Fig. S4 in the SI. Because USANS was included in these calculations, any scattering in the low Q range must be associated either with this roughness or with pores far outside of the nanopore region of concern, making the unclear source of this scattering less of a concern.

The MaxEnt calculation of the PDF, discussed in more detail in the SI, starts with the notion of a distribution that encodes our knowledge of the model before consideration of the SANS/USANS data. Although we know something about this distribution from other data, in our procedure we assume complete ignorance and chose a flat distribution over logarithmic-scaled R-bins. This is our guess of the PDF, to which the MaxEnt procedure will default in the absence of the SANS/USANS data. The values of the flat distribution are determined by least-squares fit so that the goodness of fit, $\chi^2 \approx$ N, the number of data points. There is an entropy, S, associated with the default distribution, which in Irena is computed from the Skilling and Bryan (Skilling and Bryan, 1984) "sky background", A. While the program fits this value to be about 0.01 of the maximum level of the initial featureless size distribution (on the order of $\sim 10^{-6}$ in our case) as a default, it is known that the choice of A influences the MaxEnt PDF calculation, particularly where the number of parameters, M, is of order N, which is the case here. When we overrode the default value for A over the domain 10^{-8} to 0.1, we found that more structure results in the PDF when a low sky background is assigned compared with a higher one. This is not surprising, as a high value lends more credence to the structure-less default model. In principle, we can choose among the various PDFs determined from the different values for A using the relative posterior probabilities, or inferences of the PDFs result from the MaxEnt solutions, as (Sivia and Skiolling, 2006),

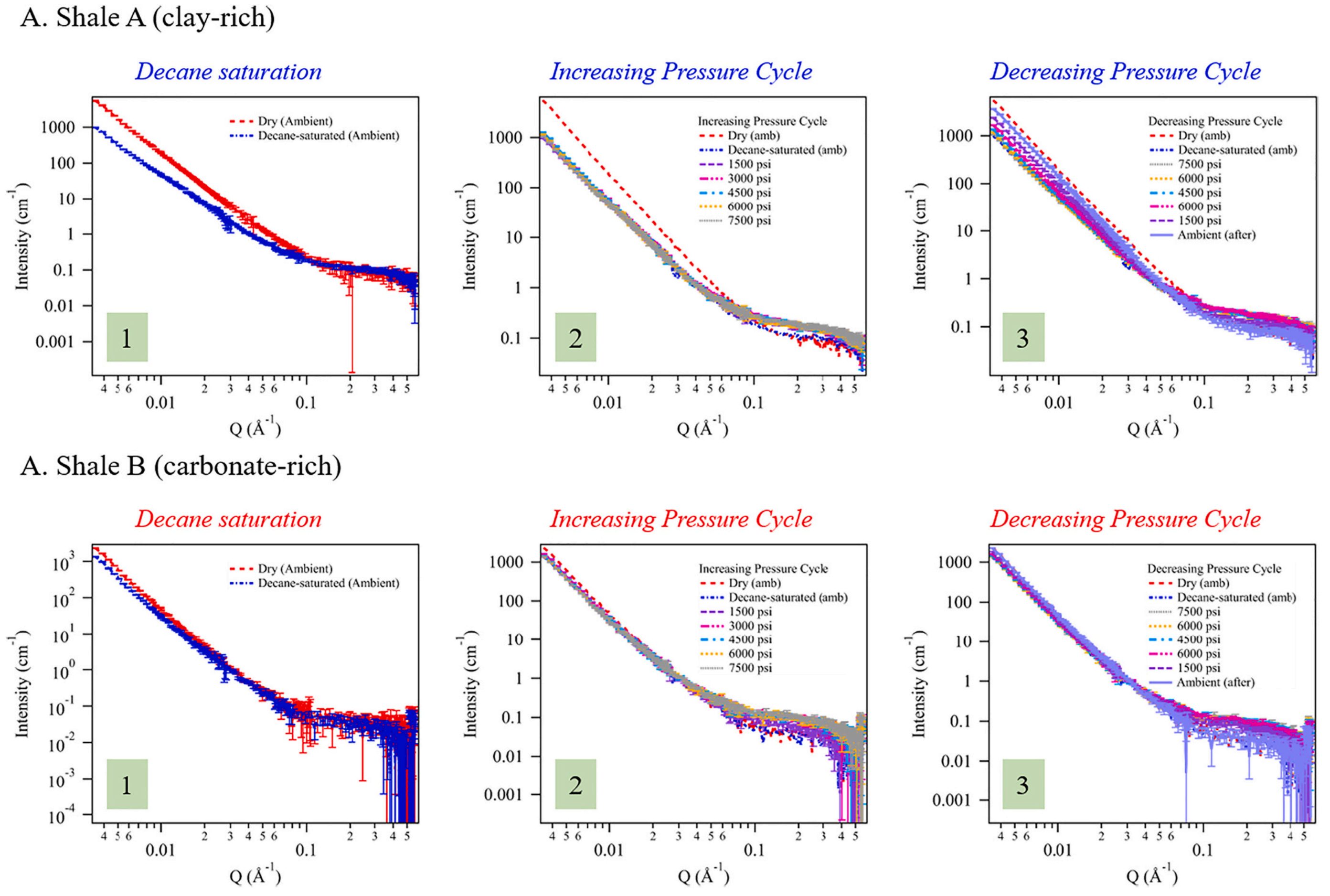

Fig. 2. SANS profiles for (A) clay-rich Shale A and (B) carbonate-rich Shale B showing scattering changes, from left to right, due to decane saturation, during the increasing pressure cycle, and during the decreasing pressure cycle. Lines overlap where pressure changes do not result in significant changes in scattering (i.e., during the increasing pressure cycle). Error bars, indicating measured error in scattering intensity, are included, but in some cases are smaller than the data marker. The confidence interval is the standard deviation.

$$\ln(prob(P_a(R).)\,|\{D\},I\,)\,) = K - \frac{\chi^2}{2} + \alpha S \tag{7}$$

The equation is read as the logarithm of posterior probability, given the data, {D}, and the prior information. In Eq. (7), α is the LaGrange multiplier, set so that $\chi^2 \cong N$, and K is a constant. However, in practice, the Irena algorithm generates $\alpha = 0.01$, meaning that the χ^2 dominates the inference, with little constraint by S. For this reason, we chose two sky background values which have similar posterior values to cover the domain of reasonable possibilities: the fitted sky background of $\sim 10^{-6}$ and a value two orders of magnitude higher, $\sim 10^{-4}$. See Section S3 in the SI for details.

3. Results and discussion

3.1. Characterization of clay- and carbonate-rich shales

Fig. 1 contains representative 2-D slices from the 3-D XCT reconstructions and DSC/TGA results from shale sample characterization. These results were previously published as part of a pore water accessibility study of shales from the same two cores (Neil et al., 2020a). Visual observation of XCT (Fig. 1A) shows differences in the mineralogy, namely the presence of large electron dense mineral grains, likely pyrite, in the clay-rich sample. This is consistent with the positive correlation between the content of organic matter and that of pyrite, as observed previously (Neil et al., 2020a). DSC/TGA results (Fig. 1B) show weight loss in the clay-rich sample due to pyrolysis of kerogen (broad endothermic event from ~400–670 °C), clay dehydroxylation (sharp endothermic peak at 537 °C), and the decomposition of pyrite. For carbonate-rich shale, there was only weight loss due to the decarbonation of calcite.

These observations are confirmed by quantitative X-ray diffraction (QXRD) (wt%) results (Table 1). Based on the measured compositions, SLDs for clay-rich and carbonate-rich shales were determined to be 3.81×10^{10} and 4.67×10^{10} cm^{-2}, respectively. To calculate this value, the density of mineral phases was used to calculate their percent composition by volume from the QXRD weight percentages. This volume composition was then used with the individual component SLDs to calculate an approximate overall matrix SLD. It is unlikely that interfaces between heterogeneous components in the matrix observed using XCT contribute significantly to the overall scattering intensity, as the SLDs of mineral constituents are all significantly higher than that of air.

3.2. SANS intensity changes during pressure cycling

Fig. 2 shows the SANS profiles for clay- and carbonate-rich shales imbibed to saturation with contrast-matching decane and during subsequent methane pressure cycling. For both shales, the intensity decreases over $Q < 0.1$ Å^{-1} upon saturation. The decrease is greater when decane was added to the clay-rich sample, Shale A, compared with the carbonate-rich sample, Shale B. This is expected, as Shale A contains significantly more organic matter, which is known to host hydrocarbons (5% as compared with 0% for Shale B). For $Q > 0.1$ Å^{-1} there is no

A. Shale A (clay-rich)

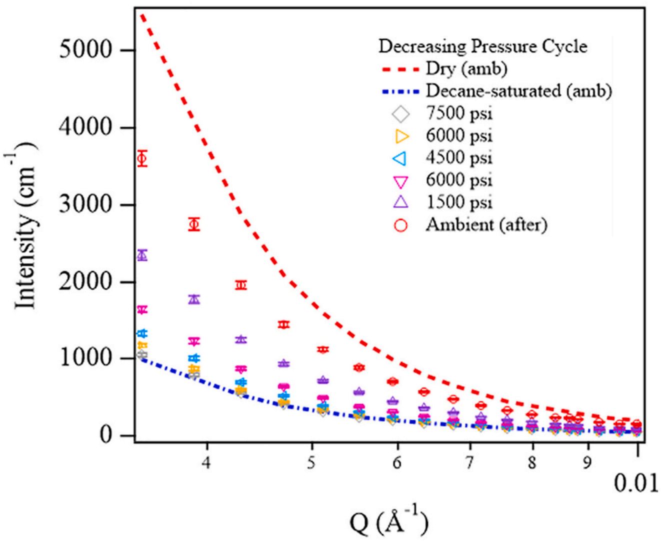

B. Shale B (carbonate-rich)

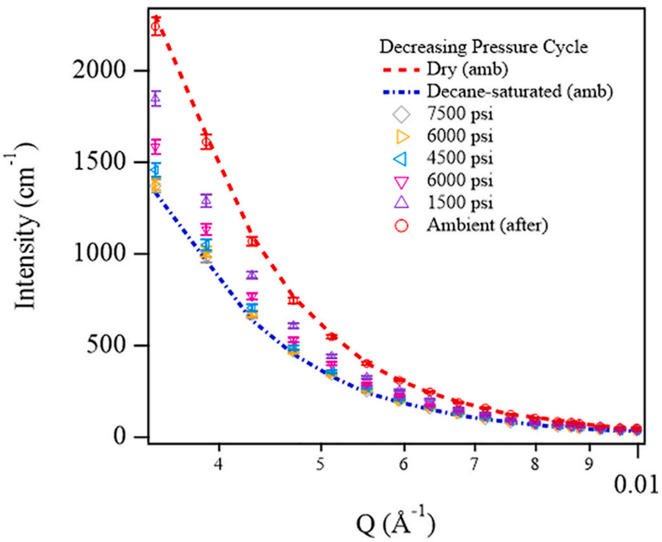

Fig. 3. Low Q SANS profiles for (A) clay-rich Shale A and (B) carbonate-rich Shale B presented with a linear intensity scale.

significant change in the intensity of either sample, indicating that the decane did not enter pores with smaller sizes.

The middle two graphs (A2 and B2) show SANS profile changes as methane pressure is increased in 1500 psi (10.3 MPa) increments from ambient to 7500 psi (51.7 MPa). In both shale samples, intensity in the lower Q region does not change significantly upon introduction of increasing pressures of methane. This result is significantly different from that of Ruppert et al. (Ruppert et al., 2013b), which showed a significant decrease in the SANS intensity with increasing CD_4 pressure. Their result was consistent with d-methane access to larger scale pores, while in our case these pores are initially filled by decane. Over $Q > 0.1$ $Å^{-1}$, there is some increase in intensity with increased pressurization with methane. A similar result of the uptake of methane was reported previously and was interpreted to be due to the formation of dense methane clusters in small shale nanopores (Ruppert et al., 2013b; Neil et al., 2020b). Without formation of these clusters, the density of CD_4 would have to be much higher than the calculated bulk SLD to cause the observed high Q intensity increase (Ruppert et al., 2013b).

In contrast, during the decreasing pressure cycle (rightmost graphs), the SANS profiles for both shale samples return towards that of the initial dry state as the pressure is decreased to ambient in 1500 psi (10.3 MPa) increments. As the CD_4 pressure is decreased, the intensity over $Q > 0.1$ $Å^{-1}$, decreases, indicating that d-methane is not retained by the smaller nanopores. In contrast, the SANS intensity above $Q \approx 0.1$ $Å^{-1}$ increased with decreasing pressure. This is consistent with removal of decane, as the largest scattering changes upon decane saturation occurred in the low Q regime. For the carbonate-rich shale, intensity nearly returns to pre-saturation values, while for the clay-rich shale, there are indications of residual decane after the pressure is returned to ambient. This is evident in Fig. 3, which presents low Q scattering profiles of the two shale samples on a linear scale.

Our observation of removal of methane in smaller nanopores during the depressurization cycle in Permian Basin shales contrasts significantly with observations from Marcellus shale. In Marcellus shale, methane retention was observed for small kerogen nanopores after depressurization from 6000 psi (41.4 MPa) (Neil et al., 2020b). Gas-generative Marcellus shale is expected to contain kerogen with a higher thermal maturity than in the Permian Basin samples used here. We expect that differences in methane retention stem from the yield strength of kerogen at different thermal maturities, which impacts the potential for non-reversible swelling deformation.

Comparison of SANS profile changes during methane depressurization provides additional insight into the pressure differential required to remove decane from shale nanopores. Fig. 4 presents the fractional decrease, calculated as the intensity decrease divided by the dry intensity at each Q value for the decane-saturated sample, the sample pressurized to 7500 psi (51.7 MPa), and each pressure decrement until reaching the final post-cycle ambient pressure condition. The low Q data clearly shows how decane removal influences the SANS profile intensity. The main conclusion from this comparison is that the pressure must drop from 7500 psi (51.7 MPa) to below 4500 psi (31.0 MPa) for significant decane removal in both shale samples. It is likely that this is the pressure where the methane-decane mixture passes below its critical point, meaning that gas and liquid phases become distinguishable and methane gas may bubble from solution, concurrently removing decane from shale pore spaces. Unfortunately, the quotients are too noisy over high Q ($Q > 0.1$ $Å^{-1}$), to draw a conclusion about relative changes over this domain with depressurization.

Our proposal that the methane-decane mixture critical point is the mechanism for decane removal is consistent with previous literature on binary methane-decane mixture critical point data taken under similar conditions. These data showed that 4500 psi (31.0 MPa) is within the range expected for the critical point of binary methane-decane mixtures. For example, Sohrabi et al. (Sohrabi et al., 2008) reported a critical point of 5300 psi (36.5 MPa) for a methane-decane mixture at 37.8 °C. Audonnet et al. (Audonnet and Pádua, 2004) reported a critical point of 35 MPa (5000 psi) for the mixture at room temperature. Herdes et al. (Herdes et al., 2015) reported a similar value at 90 °C.

Further support for this notion comes from data shown in Fig. 5, showing methane-decane phase equilibrium from experimental data and molecular dynamics simulations (Herdes et al., 2015). These results indicate that once the system pressure exceeds approximately 5000 psi (35 MPa), the amount of methane in the decane phase is maximized. When the pressure drops below this value upon depressurization, decane-laden methane vapor recondenses into a larger volume and in the process, removes decane from pore spaces. Little methane remains in the residual, non-removable decane.

3.3. Size distribution of pores retaining decane

While a qualitative interpretation of the SANS data provides insight into the relative extent of decane retention/removal between clay- and carbonate-rich shales, further analysis is needed to determine the pore

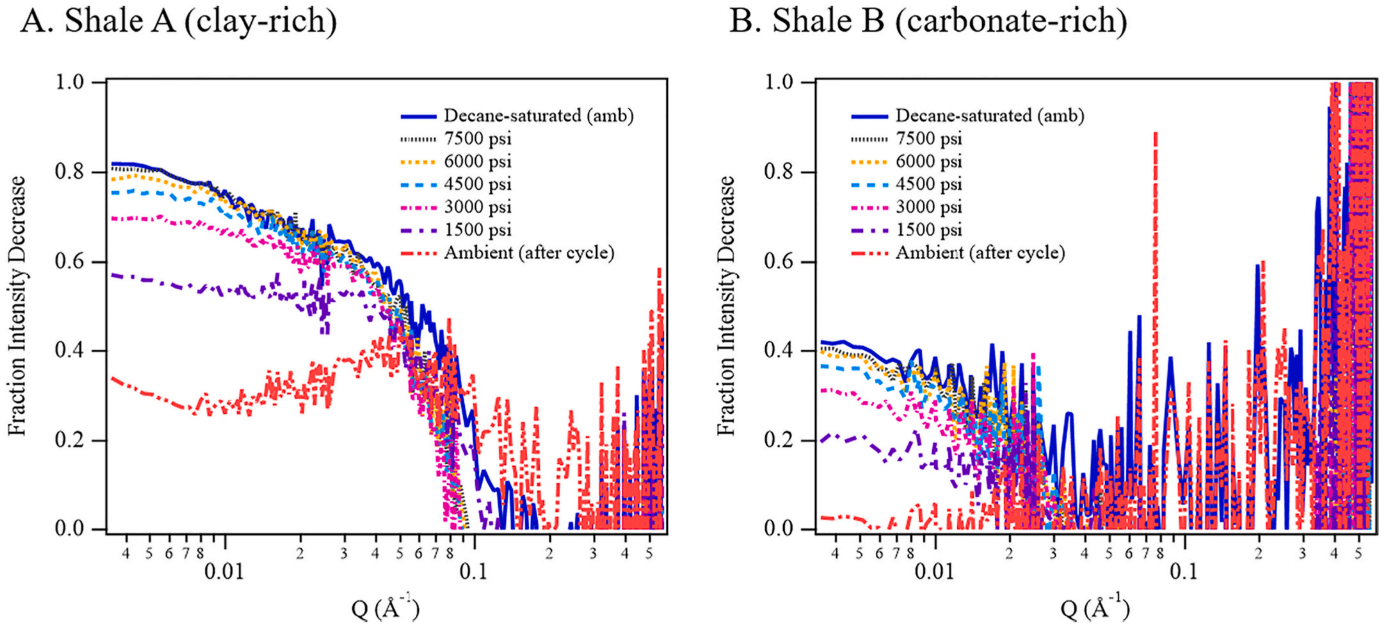

Fig. 4. Intensity decrease relative to the initial dry scattering during depressurization for (A) clay-rich Shale A and (B) carbonate-rich Shale B.

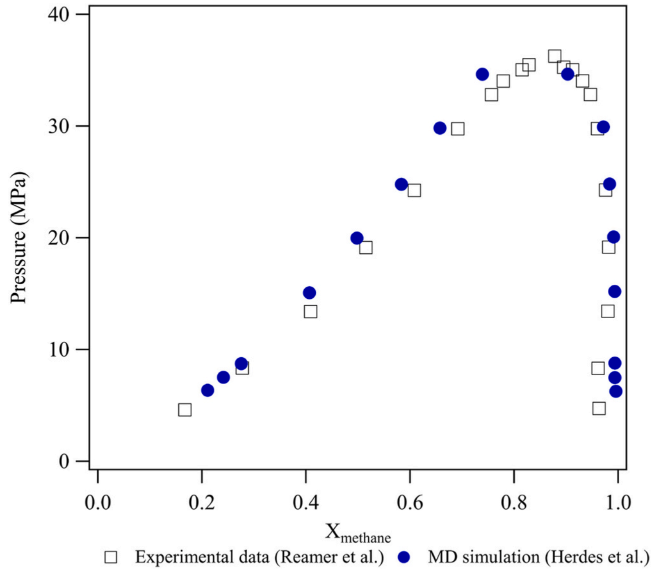

Fig. 5. Weight fraction of methane in n-decane at various pressures showing a critical point at 35 MPa for a system temperature of 363.15 K (90 °C). Reprinted with permission from Herdes et al. (Herdes et al., 2015) Experimental data is from Reamer et al. (Reamer et al., 1942)

sizes over which decane is retained. For this analysis, combined SANS and USANS intensities for ambient, decane-saturated, and post-pressure cycle conditions (Fig. 6), as expressed by Eqs. (3)–(5), were inverted to calculate the apparent PDF, $P_A(R)$, using the Irena size distribution tool with Maximum Entropy (MaxEnt) method as described in the Experimental Methods section and section S3 in the SI (Ilavsky and Jemian, 2008).

Fig. 6 presents the combined SANS and USANS scattering intensities. The dashed lines indicates the calculated intensities using the fitted pore size distributions for the two sky background values. Fig. 7 presents the log-log PDFs, $P_R(R)$, obtained for the dry sample and the apparent PDFs, $P_A(R)$, for the decane-saturated and post-pressure states of shales A and B using both the low and high sky parameter values. The comparison between $P_R(R)$, determined from the dry samples, n-decane saturated samples and post pressure cycle samples, all at ambient pressure, gives $\overline{\Delta\rho^2(R)}$ (Eq. (2)), the radial distribution and extent to which pores are filled. The SLD of deuterated methane at ambient pressure is only 0.007×10^{10} cm^{-2}, meaning that residual methane gas in the post-pressure cycle system is not expected to significantly change the USANS/SANS signal. Scattering in all three systems is thus assumed to result solely from empty pores, since decane is contrast-matched to the shale matrices.

Comparing between the results from different sky background values, there are two main differences. The first is that for the low sky background, there are more fluctuations in the data, as anticipated, even after smoothing with Igor's built in algorithm. In both cases, the PDFs are bounded at small and large *R*, where at large-*R* the data is limited by the minimum usable *Q* from the USANS measurement and at small-*R* the result is limited to $R = 1$ nm, determined by the Q value where incoherent scattering limits information on the size distributions The second difference is that the PDF for the low sky background value shows a peak at small-*R* near the minimum allowed radius of 1 nm, whereas the PDFs increases monotonically, inversely with *R*, for the high sky background value. A recent publication on this topic by Wang et al. (Wang et al., 2020) found similar differences at low *R*, with more general agreement at larger pore sizes. Although we have no valid case for discriminating between these possible models, distinct similarities exist between the PDFs with different sky backgrounds.

For both sky background values, and similarly to our previously analyzed clay- and carbonate-rich shales, the clay-rich Shale A had a narrower size distribution and smaller pores than the carbonate-rich Shale B, which had a bump in PDF between 10 and 1000 nm (Neil et al., 2020a). For both clay-rich Shale A and carbonate-rich shale B, there was a significant increase in the abundance of extremely small, 1–2 nm pores after saturation with decane, which was seen in fitting with both sky backgrounds. However, for Shale B, the uncertainty of this peak is quite large, likely due to the low scattering and high error of SANS in this region (Fig. 2B). Our previous study indicated that these are likely to be intraparticle clay pores (Neil et al., 2020a). Due to the size of these pores, they are likely less accessible to decane, which has an end-to-end length of 0.99 ± 0.1 nm (Jang et al., 2004). Pore surface wettability (hydrophobic vs. hydrophilic) can also impact accessibility, as these very small pores are shown to be preferentially accessible to water,

A. Shale A pore size distribution fitting of combined USANS and SANS data

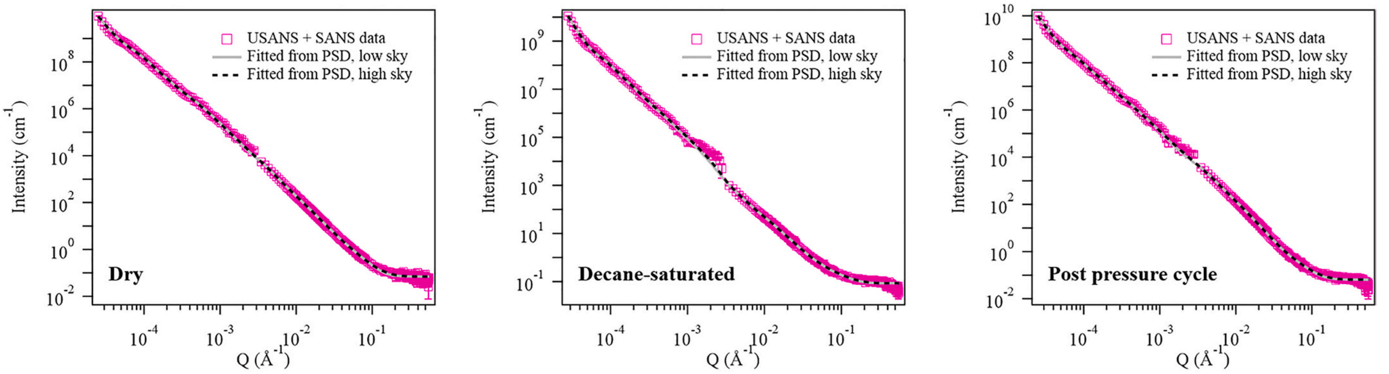

B. Shale B pore size distribution fitting of combined USANS and SANS data

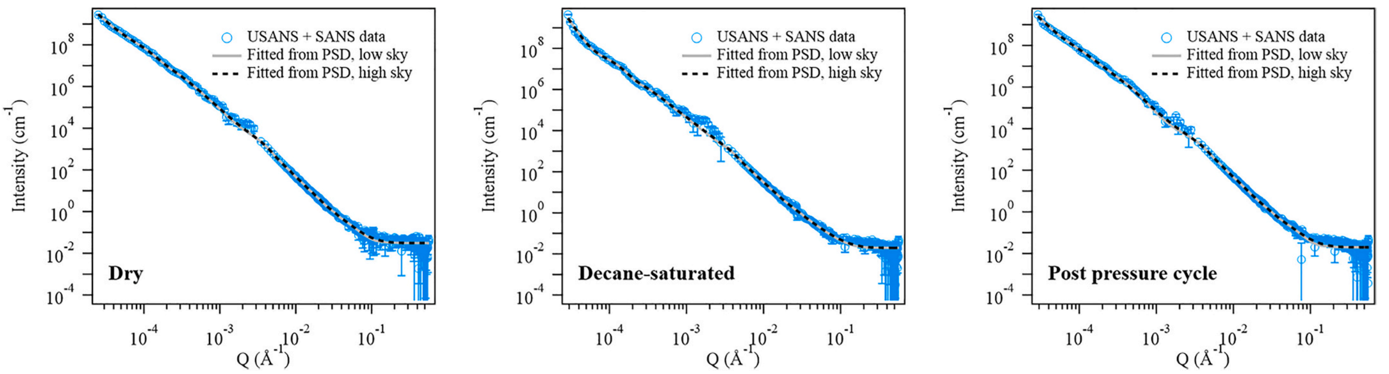

Fig. 6. Combined USANS and SANS intensity profiles for (A) clay-rich Shale A and (B) carbonate-rich Shale B under dry, decane-saturated, and post pressure cycle conditions. These profiles were fitted for pore size distribution comparison.

unlike kerogen-hosted pores (Neil et al., 2020a).

For clay-rich Shale A, there was also a significant drop in the PDF upon decane saturation for pores 3–100 nm in radius, indicating that these pores are filled by decane. For carbonate-rich Shale B, there was a slight drop in PSD between 10 and 100 nm and a more significant drop between 100 and 1000 nm. After depressurization back to ambient, the pore size distribution in the carbonate-rich Shale B returned nearly to its initial dry state, indicating that a large portion of the imbibed decane was removed. For the clay-rich shale, while the distribution increased for >10 nm pores and the peak size shifted to be slightly larger, there was significant retention, particularly between 3 nm –10 nm. This trend was clearly observed for both sky background values. These are likely to be the kerogen-hosted pores, which are expected to interact favorably with hydrocarbons such as decane and are much more prevalent in clay-rich shale than carbonate-rich shale based on its composition analysis (Table 1).

To confirm the validity of assumptions made by Irena's pore size distribution function, we conducted additional fitting using Irena's log normal distribution of spheres model for Shale A. These results can be found in Fig. S6 in the SI. This fitting produced very similar trends. Accessible pores were limited to pores larger than 1 nm in radius, which is consistent with the peak in 1–2 nm pores observed in the decane saturated system. Pores with trapped decane ranged from 3 nm to 100 nm in radius, with a peak at 10 nm, which is similar to the observed changes in size distribution between the saturated system and the system after methane pressurization. While this fit offers a more simplified fitting with an assumed log-normal distribution, this test shows that assumptions made in the process of fitting with Irena's pore size distribution function are valid.

3.4. Removable vs. non-removable decane-filled porosity

SANS and pore size distribution analyses both indicate that clay-rich shale retains more decane than carbonate-rich shale. However, quantitative comparison of the extent of decane recovery requires relating the USANS and SANS profile intensity with shale porosity. To accomplish this, we used the apparent Porod invariant, Z, to calculate the pore volume fraction, ϕ, as (Porod, 1982):

$$Z = \int_0^\infty Q^2 I(Q) dQ = 2\pi^2 (\Delta\rho)^2 \phi (1 - \phi) \tag{8}$$

Consistent with the previously described analysis, the invariant approach assumes a two-phase system where spherical pores are either entirely filled or entirely empty. Calculations were made using the residual intensity after subtracting the power law and background to be consistent with the interpretation of the combined USANS/SANS profile intensity. The combination of SANS and USANS to calculate the invariant has been used frequently in the literature (Bahadur et al., 2014; Bahadur et al., 2015; Radlinski et al., 2021; He et al., 2012; Zhang et al., 2019). Additionally, both background subtraction (Bahadur et al., 2014; Bahadur et al., 2015; Radlinski et al., 2021; He et al., 2012) and subtraction of power law scattering (Sridhar et al., 2014) has been applied in order to better calculate the invariant of the pores alone, with less contribution from other structures. The current SANS data presents a view of the pores that is approximately isotropic, with a small degree of anisotropy in the clay-rich Shale A; however, there is insufficient information on the inherent pore anisotropy to include it in the pore characterization (Gu and Mildner, 2016; Gu and Mildner, 2018).

The calculated invariant was cut off at a Q value of 0.35 Å^{-1}, due to the incoherent background at higher Q values. Invariant was calculated using the NCNR Analysis Macros for the measured Q region without

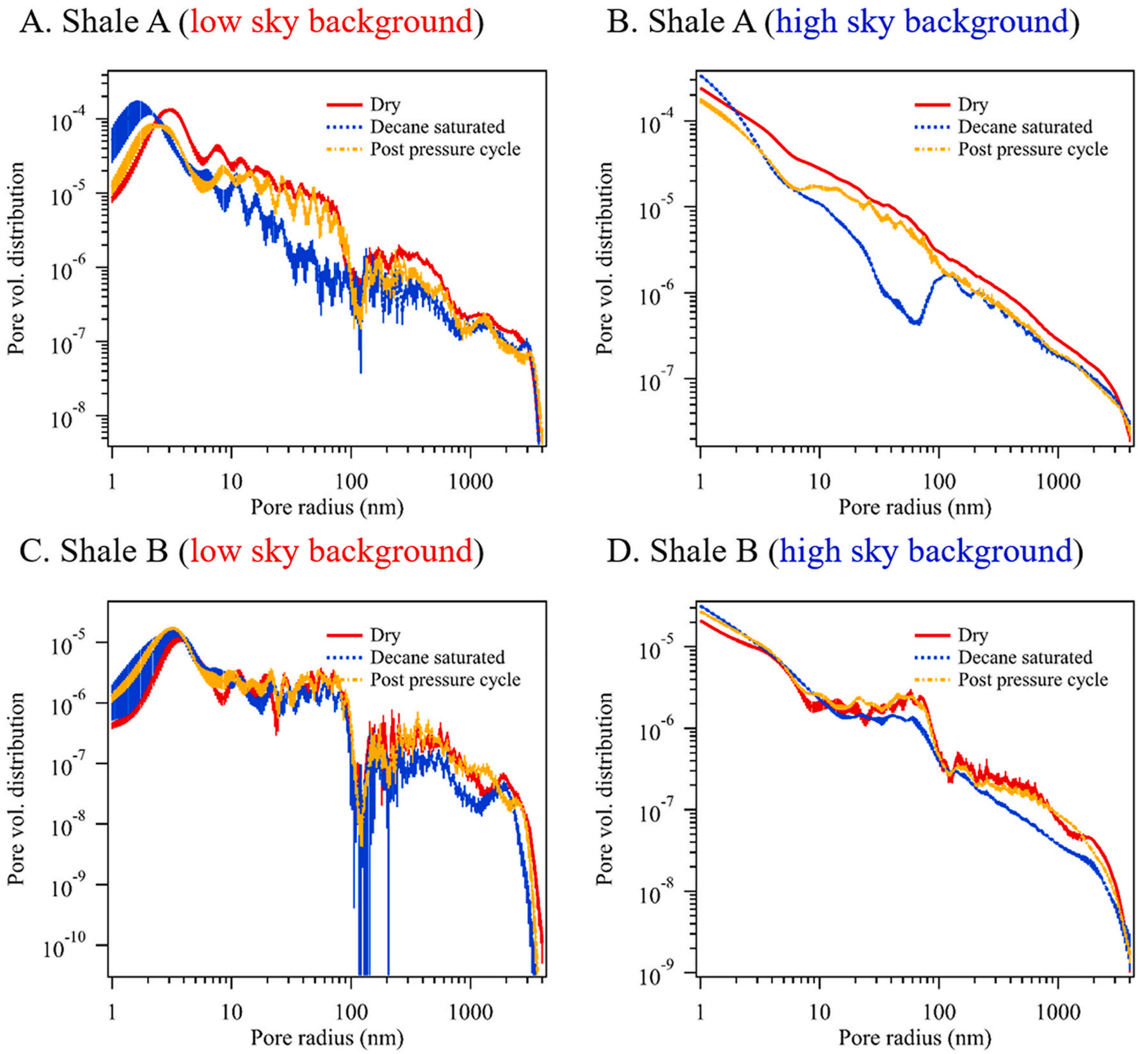

Fig. 7. Normalized pore size distributions functions (PDFs) for (A,B) clay-rich Shale A and (B,C) carbonate-rich Shale B, showing the size range where decane is retained by clay-rich shale. Fig. A and C present PDFs calculated with the low sky background, and Fig. B and D present PDFs calculated with the high sky background. Error bars represent the fitting uncertainties.

extrapolation in low or high *Q*. As this scattering is only representative of pores in the nano- to micro-scale pore size range, this porosity represents a minimum porosity present and only indicates changes in accessible porosity in the size range probed by SANS/USANS. The percent volume fraction of dry Shales A and B were calculated to be 6.71% and 1.52% respectively, aligning fairly well with previously measured values of 7.7% and 0.51%, considering the heterogeneity of shale samples and extension of porosity calculation into the USANS range (Neil et al., 2020a). Upon saturation with decane, unfilled porosity decreased to 3.41% in Shale A and 1.09% in Shale B. After depressurization, unfilled porosity increased to 4.15% in Shale A and 1.48% in Shale B.

Fig. 8 summarizes the porosity results in terms of percentages of the total porosity in each sample inaccessible to decane, filled with non-removable decane, or filled with removable decane. The key takeaways from this calculation are that for clay-rich shale, nearly 50% of the porosity was accessible to decane, while for carbonate-rich shale, only approximately 30% was accessible (Fig. 7A). For carbonate-rich shale, more than 90% of the decane-filled porosity was removable by methane pressure cycling, while for clay-rich shale, only about 20% of the filled porosity was removable. This non-removable decane is likely reside in 3–10 nm radius pores, as these pores were observed to retain decane in the pore size distribution analysis. Although this may seem to indicate that more decane is removed from the carbonate-rich shale, the porosity of clay-rich shale is significantly higher than carbonate-rich shale. Multiplying the percentage of porosity filled by removable decane with the total porosity gives comparable quantities of decane removed in Shale A and Shale B of 0.73% and 0.39%, respectively, as shown in Fig. 7B. Thus, lower porosity and less imbibition of decane in carbonate-rich Shale B results in less decane recovery than in Shale A, despite the imbibed decane being more removable.

4. Conclusions and impact

Through our in situ SANS/USANS study, we have shown that clay-rich shale has significantly more decane retention in small nanopores than carbonate-rich shale. The majority of these nanopores fall in the range of 3–10 nm in radius, and are likely hosted by organic shale components, such as kerogen. Porosity measurements show that clay-rich shale is significantly more accessible to decane than carbonate rich shale. However, while more than 90% of decane was removable in the carbonate-rich system, only approximately 20% was removable in the clay-rich system. This likely stems from differences in the wettability of pore host material, as clay-rich shale is also rich in kerogen, which will interact more favorably with hydrocarbon fluids.

This study provides several key new insights which can be used to

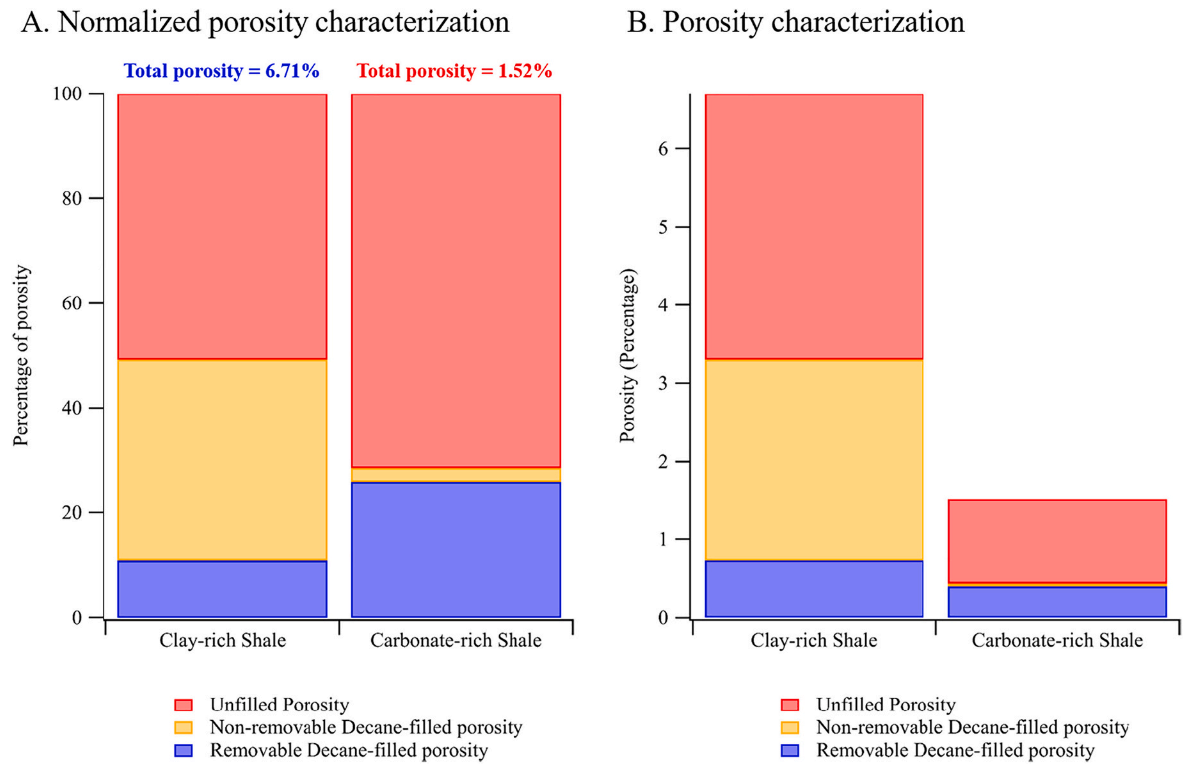

Fig. 8. Normalized (A) and non-normalized (B) characterization of clay-rich Shale A and carbonate-rich Shale B porosity as percent of n-decane filled pore and percent of pores with removable n-decane by methane pressure cycling.

inform recovery analysis in clay- or carbonate-rich strata within a given shale formation. The first is the importance of considering pressure operations relative to the phase behavior of the injectant-oil mixture, as this impacts gas evolution and transport during depressurization. The second key insight is that decane recoverability is not necessarily correlated with the degree of decane saturation. Although clay- and organic matter-rich shale had a much higher porosity and more significant imbibition of decane, a small percentage of the decane was recoverable relative to carbonate-rich shale. Many formations contain mixed lithologies, complicating analysis of recovery percentages. This new work gives insight into how recovery can vary across a formation, which may contain regions that are clay-rich and regions that are carbonate-rich.

Lastly, this study has proved the viability of SANS as a probe for fluid behavior in nanopores during primary recovery. It is recommended that future studies take advantage of this novel technique to explore EOR strategies, such as pressure cycling, exploring other injectants (e.g. supercritical CO_2) and studying recovery in additional shale lithologies. By furthering our understanding of shale response to pressure depletion and pressure cycling to improve hydrocarbon recovery, we can achieve more sustainable and economical harvesting of this valuable resource.

CRediT authorship contribution statement

Chelsea W. Neil: Investigation, Formal analysis, Writing – original draft. **Rex P. Hjelm:** Methodology, Investigation, Formal analysis, Writing – review & editing. **Marilyn E. Hawley:** Investigation, Writing – review & editing. **Erik B. Watkins:** Investigation, Writing – review & editing. **Cody Cockreham:** Investigation, Writing – review & editing. **Di Wu:** Supervision, Writing – review & editing. **Yimin Mao:** Supervision, Resources, Writing – review & editing. **Michael Cheshire:** Project administration, Funding acquisition, Writing – review & editing. **Jon Burger:** Project administration, Funding acquisition, Writing – review & editing. **Timothy B. Fischer:** Project administration, Funding acquisition, Writing – review & editing. **M. Rebecca Stokes:** Project administration, Funding acquisition, Writing – review & editing. **Hongwu Xu:** Project administration, Funding acquisition, Methodology, Conceptualization, Writing – review & editing.

Declaration of Competing Interest

The authors declare that they have no known competing financial interests or personal relationships that could have appeared to influence the work reported in this paper.

Acknowledgements

This work was supported by the Chevron Technical Center, a division of Chevron USA, through a cooperative research and development agreement (CRADA) to the Los Alamos National Laboratory (LANL) (Project PIs: Michael Cheshire and Hongwu Xu). LANL is operated by Triad National Security, LLC, for the National Nuclear Security Administration of U.S. Department of Energy (Contract No. 89233218NCA000001). The authors acknowledge the Center for Neutron Research (CNR) at National Institute of Standards and Technology for access to Small Angle Neutron Scattering (SANS). Access to Ultra-Small Angle Neutron Scattering (USANS) was provided by the Center for High Resolution Neutron Scattering, a partnership between the National Institute of Standards and Technology and the National Science Foundation under Agreement No. DMR-1508249. Di Wu acknowledges the institutional funds from the Gene and Linda Voiland School of Chemical Engineering and Bioengineering, and the fund of Alexandra Navrotsky Institute for Experimental Thermodynamics at Washington State University.

Appendix A. Supplementary data

Supplementary data to this article can be found online at https://doi.org/10.1016/j.coal.2022.103950.

References

Audonnet, F., Pádua, A.A., 2004. Viscosity and density of mixtures of methane and n-decane from 298 to 393 K and up to 75 MPa. Fluid Phase Equilib. 216 (2), 235–244.

Aycaguer, A.C., Lev-On, M., Winer, A.M., 2001. Reducing carbon dioxide emissions with enhanced oil recovery projects: a life cycle assessment approach. Energy Fuel 15 (2), 303–308.

Bahadur, J., Melnichenko, Y.B., Mastalerz, M., Furmann, A., Clarkson, C.R., 2014. Hierarchical pore morphology of cretaceous shale: a small-angle neutron scattering and ultrasmall-angle neutron scattering study. Energy Fuel 28 (10), 6336–6344.

Bahadur, J., Radlinski, A.P., Melnichenko, Y.B., Mastalerz, M., Schimmelmann, A., 2015. Small-angle and ultrasmall-angle neutron scattering (SANS/USANS) study of New Albany Shale: a treatise on microporosity. Energy Fuel 29 (2), 567–576.

Barker, J.G., Glinka, C.J., Moyer, J.J., Kim, M.H., Drews, A.R., Agamalian, M., 2005. Design and performance of a thermal-neutron double-crystal diffractometer for USANS at NIST. J. Appl. Crystallogr. 38 (6), 1004–1011.

Cardott, B.J., 2012. Thermal maturity of Woodford Shale gas and oil plays, Oklahoma, USA. Int. J. Coal Geol. 103, 109–119.

Clarkson, C.R., Solano, N., Bustin, R.M., Bustin, A.M.M., Chalmers, G.R.L., He, L., Melnichenko, Y.B., Radliński, A.P., Blach, T.P., 2013. Pore structure characterization of North American shale gas reservoirs using USANS/SANS, gas adsorption, and mercury intrusion. Fuel 103, 606–616.

Dembicki, H., 2016. Practical Petroleum Geochemistry for Exploration and Production. Elsevier.

Dong, Z., Holditch, S., McVay, D., 2013. Resource evaluation for shale gas reservoirs. SPE Econom. Manag. 5 (01), 5–16.

Glinka, C.J., Barker, J.G., Hammouda, B., Krueger, S., Moyer, J.J., Orts, W.J., 1998. The 30 m small-angle neutron scattering instruments at the National Institute of Standards and Technology. J. Appl. Crystallogr. 31 (3), 430–445.

Gu, X., Mildner, D.F.R., 2016. Ultra-small-angle neutron scattering with azimuthal asymmetry. J. Appl. Crystallogr. 49 (3), 934–943.

Gu, X., Mildner, D.F.R., 2018. Determination of porosity in anisotropic fractal systems by neutron scattering. J. Appl. Crystallogr. 51, 175–184.

Gu, X., Cole, D.R., Rother, G., Mildner, D.F., Brantley, S.L., 2015. Pores in Marcellus shale: a neutron scattering and FIB-SEM study. Energy Fuel 29 (3), 1295–1308.

Gu, X., Mildner, D.F., Cole, D.R., Rother, G., Slingerland, R., Brantley, S.L., 2016. Quantification of organic porosity and water accessibility in Marcellus shale using neutron scattering. Energy Fuel 30 (6), 4438–4449.

Guo, X., Xu, H., 2017. Enthalpies of formation of polyhalite: a mineral relevant to salt repository. J. Chem. Thermodyn. 114, 44–47.

He, L., Melnichenko, Y.B., Mastalerz, M., Sakurovs, R., Radlinski, A.P., Blach, T., 2012. Pore accessibility by methane and carbon dioxide in coal as determined by neutron scattering. Energy Fuel 26 (3), 1975–1983.

Herdes, C., Totton, T.S., Müller, E.A., 2015. Coarse grained force field for the molecular simulation of natural gases and condensates. Fluid Phase Equilib. 406, 91–100.

Hirono, T., Sakaguchi, M., Otsuki, K., Sone, H., Fujimoto, K., Mishima, T., Lin, W., Tanikawa, W., Tanimizu, M., Soh, W., Yeh, E.C., 2008. Characterization of slip zone associated with the 1999 Taiwan Chi-Chi earthquake: X-ray CT image analyses and microstructural observations of the Taiwan Chelungpu fault. Tectonophysics 449 (1–4), 63–84.

Hjelm, R.P., Taylor, M.A., Frash, L.P., Hawley, M.E., Ding, M., Xu, H., Barker, J., Olds, D., Heath, J., Dewers, T., 2018. Flow-through compression cell for small-angle and ultra-small-angle neutron scattering measurements. Rev. Sci. Instrum. 89 (5), 055115.

Ilavsky, J., Jemian, P.R., 2008. Irena and Indra SAXS Data Analysis Macros, Including Maximum Entropy. https://usaxs.xray.aps.anl.gov/software/irena.

Jang, S.S., Lin, S.T., Maiti, P.K., Blanco, M., Goddard, W.A., Shuler, P., Tang, Y., 2004. Molecular dynamics study of a surfactant-mediated decane− water interface: effect of molecular architecture of alkyl benzene sulfonate. J. Phys. Chem. B 108 (32), 12130–12140.

Jarvie, D.M., 1991. Chapter 11: Total organic carbon (TOC) analysis. In: Merrill, R. (Ed.), Treatise of Petroleum Geology: Handbook of Petroleum Geology, Source and Migration Processes, and Education Techniques. American Association of Petroleum Geologists, Tulsa, Oklahoma, pp. 113–118.

Kerr, R.A., 2010. Natural gas from shale bursts onto the scene. Science 328 (5986), 1624–1626.

Kilian, L., 2016. The impact of the shale oil revolution on US oil and gasoline prices. Rev. Environ. Econ. Policy 10 (2), 185–205.

King Jr., H.E., Eberle, A.P., Walters, C.C., Kliewer, C.E., Ertas, D., Huynh, C., 2015. Pore architecture and connectivity in gas shale. Energy Fuel 29 (3), 1375–1390.

Kline, S.R., 2006. Reduction and analysis of SANS and USANS data using IGOR Pro. J. Appl. Crystallogr. 39 (6), 895–900.

Kuuskraa, V.A., Godec, M.L., Dipietro, P., 2013. CO_2 utilization from “next generation” CO2 enhanced oil recovery technology. Energy Procedia 37, 6854–6866.

Ma, Y., Jamili, A., 2016. Modeling the density profiles and adsorption of pure and mixture hydrocarbons in shales. J. Unconvent. Oil Gas Res. 14, 128–138.

Mang, J.T., Skidmore, C.B., Hjelm, R.P., Howe, P.M., 2000. Application of small-angle neutron scattering to the study of porosity in energetic materials. J. Mater. Res. 15 (5), 1199–1208.

Mastalerz, M., He, L., Melnichenko, Y.B., Rupp, J.A., 2012. Porosity of coal and shale: Insights from gas adsorption and SANS/USANS techniques. Energy Fuel 26 (8), 5109–5120.

Melzer, L.S., 2012. Carbon dioxide enhanced oil recovery (CO_2 EOR): Factors involved in adding carbon capture, utilization and storage (CCUS) to enhanced oil recovery. Center Clim. Energy Sol. 1–17.

Neil, C.W., Hjelm, R.P., Hawley, M.E., Watkins, E.B., Cockreham, C.B., Wu, D., Mao, Y., Fischer, T.B., Stokes, M.R., Xu, H., 2020a. Small-angle neutron scattering (SANS) characterization of clay-and carbonate-rich shale at elevated pressures. Energy Fuel 34 (7), 8178–8185.

Neil, C.W., Mehana, M., Hjelm, R.P., Hawley, M.E., Watkins, E.B., Mao, Y., Viswanathan, H., Kang, Q., Xu, H., 2020b. Reduced methane recovery at high pressure due to methane trapping in shale nanopores. Commun. Earth Environ. 1 (1), 1–10.

Orr, J.F., Taber, J.J., 1984. Use of carbon dioxide in enhanced oil recovery. Science 224 (4649), 563–569.

Paltsev, S., Jacoby, H.D., Reilly, J.M., Ejaz, Q.J., Morris, J., O’Sullivan, F., Rausch, S., Winchester, N., Kragha, O., 2011. The future of US natural gas production, use, and trade. Energy Policy 39 (9), 5309–5321.

Porod, G., 1982. General theory. In: Glatter, O., Kratky, O. (Eds.), Small Angle X-ray Scattering. Academic Press, London, pp. 17–51.

Radlinski, A.P., Blach, T., Vu, P., Ji, Y., de Campo, L., Gilbert, E.P., Regenauer-Lieb, K., Mastalerz, M., 2021. Pore accessibility and trapping of methane in Marcellus shale. Int. J. Coal Geol. 248, 103850.

Reamer, H.H., Olds, R.H., Sage, B.H., Lacey, W.N., 1942. Phase equilibria in hydrocarbonsystems. Ind. Eng. Chem. 34 (12), 1526–1531.

Ruppert, L.F., Sakurovs, R., Blach, T.P., He, L., Melnichenko, Y.B., Mildner, D.F., Alcantar-Lopez, L., 2013a. A USANS/SANS study of the accessibility of pores in the Barnett Shale to methane and water. Energy Fuel 27 (2), 772–779.

Ruppert, L.F., Sakurovs, R., Blach, T.P., He, L., Melnichenko, Y.B., Mildner, D.F., Alcantar-Lopez, L., 2013b. A USANS/SANS study of the accessibility of pores in the Barnett Shale to methane and water. Energy Fuel 27 (2), 772–779.

Sivia, D.S., Skiolling, J., 2006. Data Analysis, A Baysian Tutorial, 2nd ed. Oxford University Press, Oxford.

Skilling, J., Bryan, R.K., 1984. Maximum entropy image reconstruction-general algorithm. Mon. Not. R. Astron. Soc. 211, 111.

Sohrabi, M., Danesh, A., Jamiolahmady, M., 2008. Visualisation of residual oil recovery by near-miscible gas and SWAG injection using high-pressure micromodels. Transp. Porous Media 74 (2), 239–257.

Sridhar, M., Reddy, G.K., Hu, N., Motahari, A., Schaefer, D.W., Thiel, S.W., Smirniotis, P. G., 2014. Preparation, characterization and lysozyme immobilization studies on siliceous mesocellular foams: effect of precursor chemistry on pore size, wall thickness and interpore spacing. Microporous Mesoporous Mater. 190, 215–226.

Teklu, T.W., Alharthy, N., Kazemi, H., Yin, X., Graves, R.M., AlSumaiti, A.M., 2014. Phase behavior and minimum miscibility pressure in nanopores. SPE Reserv. Eval. Eng. 17 (03), 396–403.

Tissot, B., Durand, B., Espitalie, J., Combaz, A., 1974. Influence of nature and diagenesis of organic matter in formation of petroleum. AAPG Bull. 58 (3), 499–506.

US Energy Information Administration, 2019. Annual Energy Outlook 2019: With Projections to 2050. Government Printing Office.

Van Bergen, F., Gale, J., Damen, K.J., Wildenborg, A.F.B., 2004. Worldwide selection of early opportunities for CO2-enhanced oil recovery and CO_2-enhanced coal bed methane production. Energy 29 (9–10), 1611–1621.

Wang, Q., Chen, X., Jha, A.N., Rogers, H., 2014. Natural gas from shale formation–the evolution, evidences and challenges of shale gas revolution in United States. Renew. Sust. Energ. Rev. 30, 1–28.

Wang, Y., Zhu, Y., Zhang, R., Anovitz, L.M., Bleuel, M., Liu, S., Chen, S., 2020. SANS coupled with fluid invasion approaches for characterization of overall nanopore structure and mesopore connectivity of organic-rich marine shales in China. Int. J. Coal Geol. 217, 103343.

Xu, H., 2020. Probing nanopore structure and confined fluid behavior in shale matrix: a review on small-angle neutron scattering studies. Int. J. Coal Geol. 217, 103325.

Xu, H., Navrotsky, A., Nyman, M.D., Nenoff, T.M., 2000. Thermochemistry of microporous silicotitanate phases in the Na2O–Cs2O–SiO2–TiO2–H2O system. J. Mater. Res. 15 (3), 815–823.

Xu, H., Zhang, Y., Navrotsky, A., 2001. Enthalpies of formation of microporous titanosilicates ETS-4 and ETS-10. Microporous Mesoporous Mater. 47 (2–3), 285–291.

Zhang, Y., Barber, T.J., Hu, Q., Bleuel, M., El-Sobky, H.F., 2019. Complementary neutron scattering, mercury intrusion and SEM imaging approaches to micro-and nano-pore structure characterization of tight rocks: a case study of the Bakken shale. Int. J. Coal Geol. 212, 103252.